Comparative Study of Using Superhydrophobic and Icephobic Surface Coatings for Aircraft Icing Mitigation

Haiyang Hu,* Linchuan Tian,† Chukwudum Eluchie,‡ Harsha Sista,‡ and Hui Hu§
Iowa State University, Ames, Iowa 50010

https://doi.org/10.2514/1.J063579

We report a comparative study to evaluate the effects of surface coatings with different hydrophobicities and icephobicities on the performance of a hybrid anti-/de-icing system that integrates surface heating with hydro-/ice-phobic coating for aircraft icing mitigation. While a flexible electric film heater wrapped around the leading edge of an airfoil/wing model was used to heat the airfoil frontal surface to prevent ice accretion near the airfoil leading edge, three different kinds of coatings were applied to coat the airfoil model at three distinct spanwise locations, which included an icephobic coating with an outstanding icephobicity but a weak hydrophobicity; a superhydrophobic surface (SHS) coating with outstanding water repellency but a moderate icephobicity; and a commonly used hydrophilic coating with poor hydrophobicity and poor icephobicity. Surface wettability was found to play a more important role than icephobicity in affecting the performance of the hybrid anti-/de-icing systems. In comparison to the approach of forceful heating the hydrophilic airfoil surface, the hybrid approach with the SHS coating was found to be able to achieve about 90% energy savings in keeping the entire airfoil surface ice-free; the corresponding energy savings for the hybrid system with the icephobic coating was only about 10%.

I. Introduction

AIRCRAFT icing is one of the most dangerous weather hazards faced by the aviation industry [1–8]. Aircraft in-flight icing occurs when airborne, supercooled water droplets, which make up clouds, mist, and fog, freeze into ice upon impacting airframe surfaces. Ice accretion would result in changes to the deliberately designed profiles of aircraft key components, such as wings, rudders, tailplanes, propellers, and aeroengine fan blades. Even a thin layer of ice accreted on the key components can lead to serious aerodynamic performance degradation, posing a significant risk to the flight safety of the aircraft. The importance of proper icing control was highlighted by numerous deadly aircraft crashes like that that occurred at Clarence Center, New York, on February 12, 2009, with 50 fatalities in the accident of Continental Flight 3407 [9]. While considerable progress has been made to provide a better understanding of aircraft icing phenomenon, preventing the loss of control due to inflight icing remains an important unsolved problem at the top of the National Transportation Safety Board (NTSB)'s most wanted list of aviation safety improvements.

Extensive efforts have been undertaken in recent years to develop effective anti-/de-icing strategies for aircraft inflight icing prevention [10–12]. All the current anti-/de-icing systems can be classified into two categories: active and passive strategies. While active anti-/de-icing methods rely on energy inputs from external systems to actively prevent ice formation or to remove ice once it has formed on an airframe surface, passive methods take advantage of the physical properties of the airframe surfaces (e.g., applying specially designed hydro-/ice-phobic coatings/materials) either to prevent or delay the ice formation or to promote accreted ice shedding by minimizing the ice adhesion stresses to the aircraft surfaces. Commonly used active anti-/de-icing methods include spraying de-icing fluids [13], mechanical/ultrasonic-based surface deformation [14,15], and surface heating [10]. Surface heating methods such as electric-thermal heating and hot air bleeding are the most straightforward and effective ways to prevent ice formation and remove ice accretion from airframe surfaces. While electrical-thermal heating systems employ electric resistive elements embedded in or bonded to the critical airframe surfaces [16], hot air bleeding systems usually utilize the hot air from aeroengines to the airframe surfaces for icing protection [17]. More recently, a new class of plasma-based anti-/de-icing technology has also been developed for aircraft icing mitigation [18–20]. While the surface heating methods have been demonstrated to be effective for aircraft icing protection, substantial energy inputs are usually required for the anti-/de-icing operation, which would increase fuel consumption and cause economic penalties. With low installation cost and zero energy consumption, passive approaches of using hydro/-ice-phobic surface coatings have attracted increasing interest recently as viable strategies for aircraft inflight icing mitigation.

Inspired by the outstanding self-cleaning capability of lotus leaf, extensive studies have been conducted in recent years to develop coatings to make superhydrophobic surfaces (SHSs) [21,22], on which water droplets bead up with a very large contact angle (CA; i.e., $> 150°$) and drip off rapidly when the surface is slightly inclined. One attractive application of SHS, in addition to the extraordinary water repellency, is its potential to reduce snow/ice accumulation. Under frost-free environments (i.e., low-humidity conditions), SHS was found to be very promising in delaying ice formation [23], even at temperatures as low as -25 to $-30°C$ [24]. It is well known that all SHSs possess textured or rough surfaces [25,26]. When a macroscopic water droplet encounters a textured SHS, it adopts the so-called Cassie–Baxter state [27], with air trapped inside the surface textures beneath the droplet. Since the macroscopic water droplet is supported on thousands of air pockets, it beads up and displays very high CAs (typically $> 150°$ for SHS). However, microscopic water droplets can condense from the surrounding humid air within the surface textures to form a so-called Wenzel state [28], with water completely wetting the pores or asperities of the textures. For the aircraft inflight icing scenario, airborne supercooled water droplets would impact the airframe surface at high speed (i.e., typically higher than 100 m/s). The impacting water droplets would readily penetrate the surface textures to promote the transition from the Cassie–Baxter state to the fully wetted Wenzel state. Once water freezes within the textures in the Wenzel state, it would be extremely difficult to remove the ice because of the interlocking between ice and the textures [29,30]. Consequently, some SHS were found to display even higher ice adhesion strengths than

Presented as Paper 2023-4275 at the AIAA Aviation 2023 Forum, San Diego, CA, June 12–16, 2023; received 15 September 2023; revision received 30 November 2023; accepted for publication 1 December 2023; published online 26 January 2024.

*Postdoctoral, Department of Aerospace Engineering; currently Assistant Professor, Department of Mechanical and Aerospace Engineering, University of Alabama, Huntsville, AL.

†Postdoctoral, Department of Aerospace Engineering; currently, School of Aeronautics and Astronautics, Shanghai Jiao Tong University.

‡Graduate Student, Department of Aerospace Engineering.

§Martin C. Jischke Professor, Department of Aerospace Engineering; huhui@iastate.edu. Associate Fellow AIAA (Corresponding Author).

nontreated surfaces, substantially increasing the energy required to remove the accumulated ice [26,31]. In summary, SHS coatings with textured surfaces, which are effectively icephobic at nominal static icing conditions, may not perform well for aircraft inflight icing scenario involving impingement of supercooled water droplets at very high impacting speeds.

An icephobic material/surface usually refers to the material/surface that can hinder ice from forming and/or having a very small ice adhesion strength to the surface (i.e., $\tau_{ice} < 100$ kPa) [32–36]. Icephobic surfaces are usually found to show the following ice repellency, i.e., more readily shedding of water droplets via roll-off or/and rebound on the cold surface before freezing; decreasing the temperature for ice nucleation; prolonging the frosting or freezing time; and lowering the ice adhesion strength when ice accretion is inevitable [32,37,38]. Some of the commonly used icephobic materials/surfaces include Pitcher-plant-inspired slippery liquid-infused porous surfaces (SLIPS) [39–43], elastic icephobic surfaces [44,45], hydrated surfaces [46,47], and stress-localized icephobic surfaces [36,46]. It should be noted that while some of the SHS coatings are found to be icephobic (i.e., $\tau_{ice} < 100$ kPa), not all icephobic surfaces are superhydrophobic [32,48,49]. Some of the icephobic surfaces can even be hydrophilic [50].

While both hydrophobic and icephobic surface coatings have been demonstrated to have great potential for aircraft icing protection [51–54], one of the major drawbacks of the passive methods using hydrophobic or icephobic coatings is their ineffectiveness in suppressing ice accretion in the regions near airframe leading edges [51,55]. Since hydrophobic or icephobic coatings are assumed to produce low adhesion forces between the airframe surfaces and impinging water droplets or accreted ice, the passive methods rely on aerodynamic shear forces acting tangentially to the airframe surfaces to remove the impinged water droplets and accreted ice structures. Such passive strategies would become invalid at the stagnation lines because the required aerodynamic shear forces near the stagnation lines are very small or completely vanish [51,55]. While the water collection efficiency would usually be the maximum at the stagnation lines near the airframe leading edges, the impinged supercooled water droplets would accumulate and freeze into ice rapidly along the leading edges. Once ice structures start to accrete along the stagnation lines, more supercooled water droplets would impact directly onto the surfaces of the accreted ice structures, instead of the hydrophobic or icephobic airframe surfaces. This would result in more and more ice structures accreted in the region near the airframe leading edges. Therefore, an ideal solution for aircraft icing prevention would be a system with only a minimized power input to effectively delaminate the ice accretion in the required locations such as airframe leading edges, while utilizing passive hydro-/ice-phobic coatings to delay ice accretion and to promote the removal of the accreted ice with requisite aerodynamic forces exerted by the boundary-layer airflows over the airframe surfaces.

An anti-/de-icing hybrid strategy that integrates hydro-/ice-phobic coatings with limited surface heating near the airframe leading edges has been suggested recently to effectively remove ice accretion from airframe surfaces [54,55]. In comparison to conventional active methods of forceful heating the massive airframe surfaces, the hybrid anti-/de-icing strategy was found to be able to keep the entire airframe surface ice-free with substantially less power consumption [55]. While both SHS [55] and icephobic coatings [51] are found to be promising for aircraft icing prevention, much work is still needed to optimize the design paradigms of hybrid anti-/de-icing systems to minimize the power consumption required for an anti-/de-icing operation. Considering the different working mechanisms of hydrophobic coatings against icephobic coatings, a comprehensive investigation is conducted in the present study to compare their effectiveness in composing hybrid anti-/de-icing systems for aircraft icing protections. The experimental study was conducted in the Icing Research Tunnel of Iowa State University (ISU-IRT) with an airfoil/wing model exposed to a typical wet glaze icing condition. While a flexible electric film heater wrapped around the airfoil leading edge was used to actively prevent ice accretion over the airfoil frontal surface, three kinds of surface coatings with different hydrophobicities and icephobicities were applied to coat the airfoil surface at three distinct spanwise locations. The compared coatings included 1) an icephobic coating with an outstanding icephobicity but a moderate hydrophobicity; 2) an SHS coating with an outstanding hydrophobicity but a moderate icephobicity; and 3) a commonly used hydrophilic coating with a poor hydrophobicity and poor icephobicity as a comparison baseline. During the experiment, in addition to acquiring snapshot images to reveal the features of the dynamic ice accretion and anti-/de-icing processes over the airfoil surfaces coated with different coatings, a high-speed IR thermal imaging system was also used to quantify the unsteady heat transfer process over the airfoil surfaces. The snapshot images acquired during the dynamic ice accretion and anti-/de-icing process were coordinated with the quantitative IR thermal imaging results to elucidate the underlying physics to gain further insight into the working mechanisms of the hybrid anti-/de-icing systems with SHS coatings in comparison to those with icephobic coatings.

II. Experimental Setup and Test Model

A. Icing Research Tunnel and the Test Model used in the Present Study

The experimental study was performed in an Icing Research Tunnel available at Iowa State University (i.e., ISU-IRT), a newly refurbished, multifunctional icing research tunnel. As shown schematically in Fig. 1, ISU-IRT has a test section with four optically transparent sidewalls and physical dimensions of 2.0 m in length, 0.4 m in width, and 0.4 m in height. It can generate a maximum wind speed of 65 m/s with the airflow temperature cooled down to −25°C. An array of nine spray nozzles/atomizers (IKEUCHI BIMV 8002) was mounted inside the ISU-IRT to inject microsized water droplets into the airflow. Based on the measurement results of a LaVision's ParticleMaster™ system, the water droplets inside the ISU-IRT were found to range from 10 to 100 μm in size, with a mean volume diameter (MVD) of about 20 μm in the test conditions used for the present study. By manipulating the pressure and flow rate supplied to the atomizer/spray nozzles, the liquid water content (LWC) levels inside the ISU-IRT can be adjusted from 0.10 to 5.0 g/m^3. The turbulence level of the airflow at the entrance of the test section was found to be about 3.0%, as measured using a hotwire anemometer. In summary, the ISU-IRT has been used to simulate atmospheric icing phenomena under a wide range of icing conditions, i.e., from very dry rime to extremely wet glaze ice conditions representative of typical aircraft icing envelopes [56]. Further details about ISU-IRT can be found in the published literature of Liu and Hu [57].

An airfoil/wing model, which has a NACA 0012 airfoil profile in the cross section with a chord length of $C = 150$ mm and a spanwise length of $L = 400$ mm was used in the present study. It should be noted that, while traditional airplanes are typically made of *metals* (e.g., aluminum and/or aluminum alloy), modern airplanes use more and more polymer-based-composite parts. For example, a large portion of the primary structure of Boeing 787 Dreamliners is made of composite materials (i.e., 50% by weight). Furthermore, almost all unmanned aerial vehicles or drones are made of polymer-based composites. Since local heat transfer to remove the released latent heat of fusion from ice accreting surface is one of the key controlling factors to determine ice types (i.e., rime vs glaze) and ice accretion rate, the significant difference in the thermal conductivity between the metal-based traditional aircraft (i.e., ~200 W/[m · K]) and the polymer-based modern aircraft and/or UAVs (i.e., only ~0.2 W/[m · K]) would result in great differences in the ice accretion characteristics and anti-/de-icing process. While the primary objective of the present study is to explore novel anti-/de-icing strategies for modern aircraft and UAV icing protection, a polymer-based test model was used for the present study. The test model was made of a hard-plastic material (i.e., VeroWhitePlus™, Stratasys, Inc.) and manufactured by using a rapid prototyping machine (i.e., 3D printer) that builds the test models layer by layer with a resolution of about 25 μm. According to the Material Safety Data Sheet (MSDS) of hard-plastic material, the density, thermal conductivity, and specific heat coefficient of the material are 1.18 g/cm^3, 0.22 W/(m · K), and 1340 J/(kg · K), respectively.

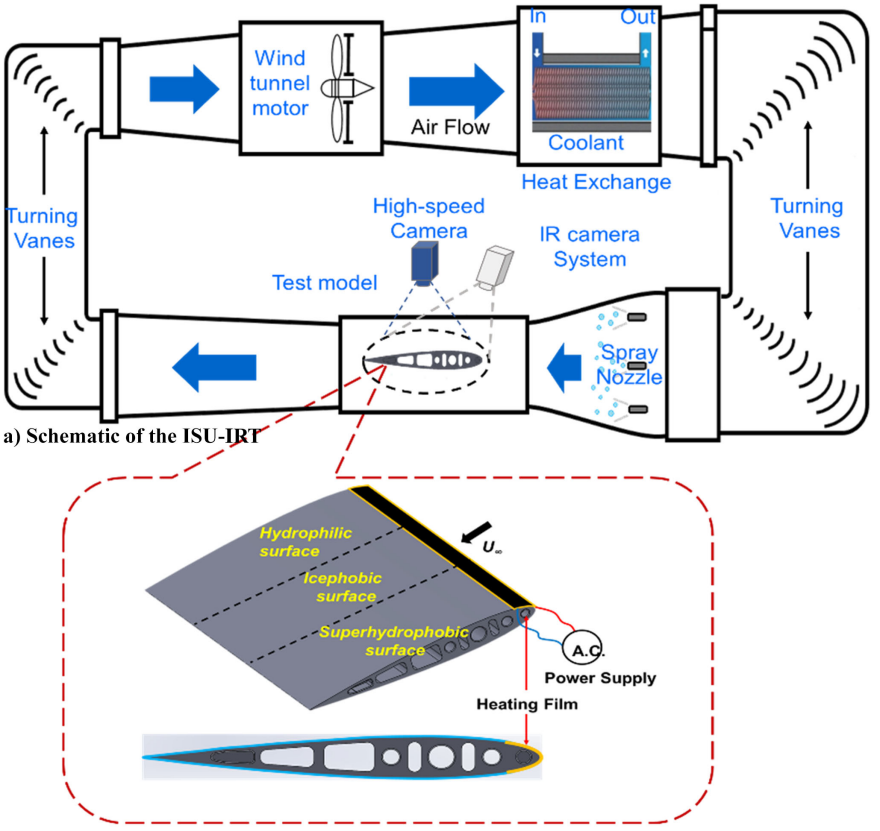

Fig. 1 Schematic of the ISU-IRT and experimental setup.

As illustrated schematically in Fig. 1, a thin, flexible electric film heater (i.e., DuPont™ Kapton® film heater with a thickness of 50 μm) was wrapped around the leading edge of the airfoil model within ~10% of the airfoil chord length (i.e., covering most entire direct impinging zone of the airborne water droplets) to provide surface heating to melt the accreted ice structures near the airfoil leading edge. The thin film heater was attached to the airfoil surface firmly with a thin layer of spray adhesive (i.e., 3M™ Super 77 Multipurpose spray adhesive). Another thin layer of Kapton® film (~50 μm in thickness) was used to cover the entire airfoil surface (i.e., on the top of the film heater) to ensure electric isolation and a smooth surface finish. Then, the airfoil surface was coated with several layers of spray-on primer (Rustoleum™ Primer) and an all-weather protective enamel painting (Rustoleum™ white Flat Protective Enamel). After applying the enamel paint, the airfoil surface was wet sanded with fine sandpapers up to 2000 grades to achieve a nearly mirror-like smooth finish.

During the experiments, the airfoil model was mounted horizontally in the ISU-IRT, and the angle of attack (AOA) of the airfoil model in relation to the incoming airflow was set to be zero (i.e., AOA = 0°). The film heater was powered using an alternative current (AC) power source along with an AC variable transformer. The electric voltage and current supplied to the film heater were measured with a digital multimeter, which were used to calculate the electric power supplied to the film heater for the anti-/de-icing operation.

B. Surface Coatings Used in the Present Study

In the present study, three kinds of surface coatings with different hydrophobicities and icephobicities were applied to coat the airfoil surface at three distinct spanwise locations. The test coatings included 1) an icephobic coating with outstanding icephobicity but weak hydrophobicity; 2) an SHS coating with outstanding hydrophobicity but moderate icephobicity; and 3) a commonly used hydrophilic coating with relatively poor hydrophobicity and icephobicity as the comparison baseline. As shown schematically in Fig. 1, a commercially available SHS coating (i.e., Rust-Oleum Neverwet® coating) was applied to cover the right 1/3 span of the test model, and an icephobic coating (i.e., Nanosonic Hybridshield® icephobic coating) was used to coat the 1/3 of the model surface at the midspan. After switching on the electric film heater wrapped around the airfoil leading edge, two hybrid anti-/de-icing systems (i.e., integrating the limited surface heating at the airfoil leading edge with either the SHS or icephobic coating) were compared side by side to evaluate their effectiveness for the aircraft icing mitigation. It should also be noted that the airfoil surface at the left 1/3 span of the test model was covered with hydrophilic enamel coating, which will be used as the baseline for the comparative study.

In the present study, a set of experiments were conducted to characterize the wettability and icephobicity of the three surface coatings. While the acquired images of water droplets sitting on the three compared surfaces for the static contact angle (CA) measurements are shown in Fig. 2, the measured wettability parameters and the ice adhesion strength on the compared surfaces are listed in Table 1 for a quantitative comparison. It should be noted that the wettability parameters (i.e., in the terms of the static CA θ_{static}, advancing CA θ_{adv}, and receding CA θ_{rec} of water droplets) of the three compared surfaced were measured by using a needle-in-the-sessile-drop method similar as that described in Korhonen et al. [58]. Further details about the experimental setup and image processing procedure for the CA measurements can be found at our published papers [51,59,60]. The ice adhesion force data were measured under a static condition by using a push-based method similar to that used in the previous studies [61,62]. The mean and standard deviation values, which were calculated based on 10 independent test trials, are also provided in Table 1.

As shown clearly in Fig. 2, while the static CA on the test surface coated with Hybridshield® coating was measured to be ~100° with the CA hysteresis (i.e., $\Delta\theta = \theta_{adv} - \theta_{rec}$) being ~50°, the ice adhesion strength was found to be only 75 kPa (i.e., τ_{ice}≈75 kPa), confirming that the icephobic coating has an outstanding icephobicity

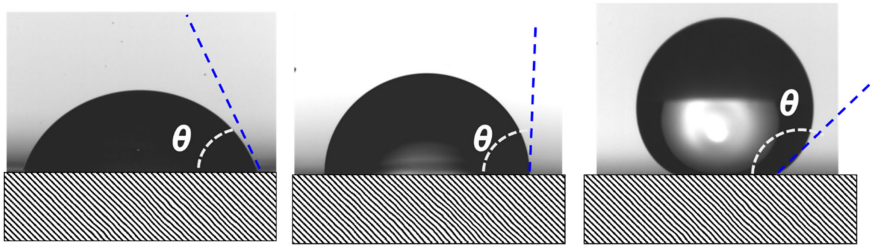

a) Hydrophiclic surface (Enamel - baseline) b) Icephobic surface (Hybridshield™) c) SHS surface (Neverwet™)

Fig. 2 Acquired images of water droplets on the compared surfaces.

Table 1 Measured contact angles and ice adhesion strength on the compared surfaces

Tested surface	Static CA, θ_{static}, °	Advancing CA, θ_{adv}, °	Receding CA, θ_{rec}, °	CA hysteresis, $\Delta\theta$, °	Ice adhesion strength, τ_{ice}, kPa (measured at −5.0°C)
Hydrophilic surface (baseline)	65 ± 2	85 ± 2	10 ± 2	∼75	510 ± 50
Icephobic surface	100 ± 2	110 ± 2	60 ± 2	∼50	75 ± 10
Superhydrophobic surface	153 ± 1	157 ± 2	152 ± 2	∼5	110 ± 20

but weak hydrophobicity. In comparison, the test surface coated with the Neverwet® SHS coating was found to have a very high static CA value of 153° and a very low CA hysteresis of ∼5°, while the corresponding ice adhesion strength on the SHS-coated surface was measured to be 110 kPa (i.e., $\tau_{ice}\approx$110 kPa), suggesting that the SHS-coated surface has an extraordinary water repellency but moderate icephobicity. However, for the enamel-coated surface (i.e., the comparison baseline), while static CA and hysteresis were about 65° and 75°, respectively, the ice adhesion strength was measured to be 510 kPa (i.e., $\tau_{ice}\approx$510 kPa), indicating that the baseline surface is hydrophilic with a poor icephobicity.

As described in Wang et al. [63], for a wind-driven water droplet moving over a test surface, the aerodynamic force exerted by the boundary-layer airflow would be counter balanced by the capillary force (i.e., the lateral adhesion force caused by the liquid surface tension on the liquid-solid-air interface). Based on the measured surface wettability parameters listed in Table 1, the capillary force to restrain a wind-driven water droplet from moving over the surfaces coated with the three compared coatings can be estimated with a theoretical model given in Waldman et al. [64] and Gao et al. [55], which is expressed as

$$F_{\text{cap.}} \approx \pi R \gamma_{LG}\left[\sin\left(\frac{\theta_{\text{adv}}-\theta_{\text{rec}}}{2}\right)\sin\left(\frac{\theta_{\text{adv}}+\theta_{\text{rec}}}{2}\right)\right] \quad (1)$$

where R is the spherical cap radius of the water droplet, and γ_{LG} is the liquid–gas surface tension at the contact line, and θ_{adv} and θ_{rec} represent the advancing and receding CAs, respectively.

With the assumption that the γ_{LG} value would not change over the three compared surfaces, the relative capillary forces experienced by the droplets with same spherical cap radii (i.e., the same R value) sitting on the icephobic or SHS-coated surface in relation to that on the hydrophilic surface (i.e., the baseline case) can be estimated by inserting the values of the measured advancing and receiving angles given in Table 1 into Eq. (1). It was found that the capillary force acting on a water droplet moving over the icephobic surface would be about 90% of that on the hydrophilic baseline surface. However, once the water droplet was frozen into ice, the adhesion force of the accreted ice to the icephobic surface (i.e., $\tau_{ice}\approx$75 kPa) would be much smaller than that on the hydrophilic baseline surface (i.e., being only ∼15% of that on the hydrophilic surface). In comparison, the capillary force acting on a water droplet on the SHS-coated surface was estimated to be only ∼4% of that on baseline hydrophilic surface, suggesting that the water droplet would be much more readily blown away by the incoming airflow from the SHS-coated surface. The ice adhesion strength on the SHS-coated surface was found to be smaller than that on the hydrophilic baseline surface (i.e., becoming ∼22% of that on the hydrophilic surface), but much greater than that on the surface coated with the icephobic coating (i.e., about 50% greater).

C. Icing Test Conditions and Measurement Systems

It is well known that, after airborne supercooled water droplets impinging onto an airframe surface to start an icing process, the freezing can be complete or partial, depending on how rapidly the latent heat of fusion can be released into the ambient airflow [51,65]. In a dry regime, all the water collected in the impingement area freezes on impact to form rime ice. For a wet regime, only a fraction of the impinged supercooled water droplets would freeze in the impingement area to form glaze ice and the remaining unfrozen water would run back and freeze subsequently outside the droplet impingement area. Mixed ice refers to the situation with simultaneous appearance of both rime and glaze ice characteristics. In comparison to the rime icing scenario, glaze icing is known to be more dangerous since it would deform the profiles of the ice accreting surface more severely because of its wet nature, i.e., forming irregular-shaped "ice horns" and larger "ice feathers" to cause a greater aerodynamic performance degradation [66–69]. It was also reported that the glaze ice would be much more difficult to remove once built up [70,71]. Therefore, a typical glaze icing condition was generated in the ISU-IRT to evaluate the performances of the hybrid anti-/de-icing systems with the airfoil surfaces covered with different coatings. More specifically, for the glaze icing experiments, while the velocity of the incoming airflow was fixed at $V_\infty = 40$ m/s, the temperature and the liquid water content (LWC) level of the incoming airflow were set to be $T_\infty = -5$°C and LWC $= 2.0$ g/m^3.

During the experiments, two sets of high-speed imaging systems (i.e., 2 FASTCAM MINI WX cameras with a maximum pixel resolution of 2048 × 2048 and a frame rate up to 10 kHz) were used to record the dynamic ice accretion and anti-/de-icing process over the airfoil surfaces treated with different coatings. While one of the imaging systems has a large observation window (i.e., ∼100 mm by 200 mm in window size) to reveal the global features of the ice accretion and anti-/de-icing process over the airfoil surface, the second system was equipped with a 8X Microlens to focus on the regions near the airfoil leading edge to provide a zoom-in view (i.e., ∼10 mm by 20 mm for the observation window) to reveal further details of the icing and anti-/de-icing process over the compared airfoil surfaces.

A high-speed infrared (IR) thermal imaging system (FLIR, A615 with 640 by 480 pixels in spatial resolution and up to 200 Hz in image acquisition frame rate) was also utilized to quantitatively measure the

surface temperature distribution over the surface of the airfoil model during the anti-/de-icing operation. For the IR thermal image acquisition, an infrared window (FLIR, IR Window-IRW-4C) was embedded into the top panel of the ISU-IRT test section. A procedure similar to that described by Liu and Hu [57] was performed to calibrate the IR thermal imaging measurement system at several prescribed temperatures (i.e., between −20.0 and 15°C) before starting the anti-/de-icing experiments. In addition, two miniature K-type thermocouples were also flush-mounted on the surface of the airfoil model to monitor the variations of the airfoil surface temperature during the experiments. The measurement results from the thermocouples and the IR thermal imaging system were found to agree well (i.e., the differences between the measurement results being less than ±1.0°C). For the test cases of the present study, the IR thermal imaging system was operated to take IR images at the frame rate of 20 Hz.

Before taking measurements, the ISU-IRT was operated at a preselected frozen cold temperature level (i.e., $T_\infty = -5$°C for the present study) for at least 30 min with the airfoil model installed in the tunnel under a dry airflow condition (i.e., before turning on the water spray system) to ensure that the ISU-IRT reached a thermally steady state. After switching on the water spray system of ISU-IRT, micro-sized water droplets injected by the water spray system in the ISU-IRT were cooled down rapidly to reach a supercooled state. Upon impinging onto the surface of the airfoil model, some of the impinged supercooled water droplets would be frozen into ice immediately to start ice accretion on the model surface.

III. Measurement Results and Discussion

A. Ice Accretion Process over the Airfoil Surfaces Treated with Different Surface Coatings

In the present study, the characteristics of the dynamic ice accretion process over the airfoil surfaces treated with different surface coatings were examined before tuning on the electric film heater for the anti-/de-icing operation. Figure 3 shows typical snapshot images to reveal the global features of the dynamic ice accretion process over the airfoil surfaces treated with different surface coatings (i.e., hydrophilic, icephobic, and SHS coatings). The zoom-in view images of the dynamic ice accretion process (i.e., within a zoom-in window near the airfoil leading edge) at the beginning of the glaze icing process (i.e., within the first 40 s) are given in Fig. 4, which reveals further details about the effects of the surface coatings on the ice accretion process. As described above, with the water spray system of ISU-IRT turning on at $t = 0$ s, the supercooled water droplets would impinge onto the airfoil surfaces to start ice accretion immediately. Corresponding to the high LWC level under the glaze icing condition

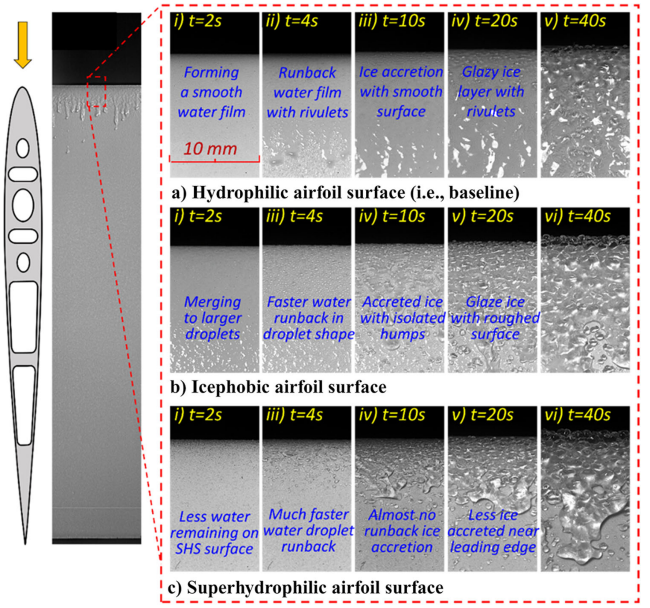

Fig. 4 Zoom-in view of the ice accretion process near the airfoil leading edge.

used for the present study (i.e., LWC $= 2.0$ g/m^3), a large amount of airborne supercooled water droplets would impinge onto the model airfoil, causing the release of a tremendous amount of latent heat of fusion over the airfoil surface associated with the solidification (i.e., icing process) of the impinged supercooled water droplets. However, the heat transfer (i.e., both convective and conductive heat transfer processes) over the airfoil surface would be insufficient to rapidly dissipate all the latent heat of fusion due to the relatively high ambient temperature under the glaze icing condition (i.e., $T_\infty = -5.0$°C), which would delay the solidification of the impinged supercooled water droplets. As a result, only a portion of the impinged supercooled water droplets would be frozen into ice immediately, while the rest of the impinged water droplets would stay in liquid phase. The unfrozen water would move freely over the airfoil surface until all the released latent heat of fusion is dissipated completely.

As revealed clearly in Fig. 4a, for the hydrophilic airfoil surface (i.e., treated with enamel coating) on the left span of the model airfoil (i.e., the baseline case), while a portion of the impinged supercooled water droplets were found to be frozen into ice immediately to cause the ice accretion along the airfoil leading edge, unfrozen water droplets were found to coalesce rapidly to form a thin water film

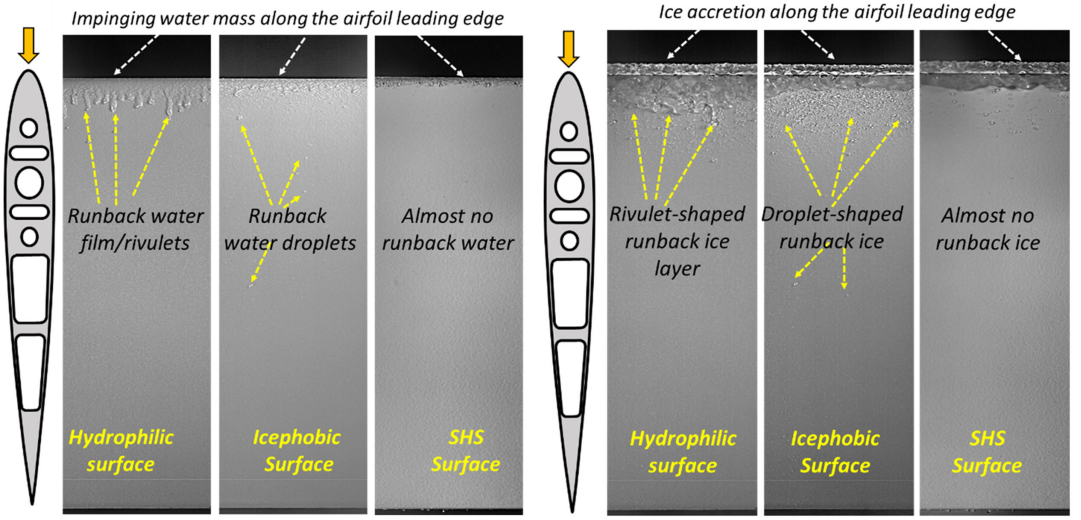

a) Acquired images at $t = 10$s **b) Acquired images at $t = 120$s**

Fig. 3 Ice accretion process over the airfoil surfaces coated with different coatings.

over the hydrophilic airfoil frontal surface (i.e., within the direct impinging zone of the airborne water droplets). Driven by the aerodynamic shear forces exerted by the incoming airflow, the unfrozen water was found to flow gradually over the ice-accreting airfoil surface, forming a runback water flow with multiple rivulets along its front contact line, as shown clearly in Fig. 4a. The wind-driven water film/rivulet flow would transport the impinged water mass from the airfoil frontal surface to further downstream locations (i.e., out of the direct impinging zone of the airborne water droplets) [72–75]. With the incoming airflow being frozen cold (i.e., $T_\infty = -5.0°C$), the runback water film/rivulet flow was cooled down continuously, and frozen into ice eventually when the released latent heat of fusion was dissipated completely, leading to the formation of rivulet-shaped runback ice structures at further downstream locations, as shown clearly in Fig. 3b. It can be clearly seen that the ice structures accreted over the hydrophilic airfoil surface are transparent with a glazy appearance, i.e., with typical features of glaze ice accretion [67,76], as expected. With increasing ice accretion time, while the thickness of the ice layer accreted along the airfoil leading edge increased monotonically due to the impingement of more supercooled water droplets, the coverage of the ice layer accreted over the airfoil surface was also found to spread continuously with the rivulet-shaped runback ice structures extending further downstream.

As revealed clearly in Fig. 4b, even though the ice adhesion strength on the icephobic airfoil surface became only about 15% of that on the hydrophilic airfoil surface, substantial ice structures were still found to accrete over the icephobic airfoil surface, primarily in the region near the airfoil leading edge. The ineffectiveness of the passive method using icephobic coating to prevent ice accretion near the airfoil leading edge is caused by the very small or even vanished aerodynamic shear stress near the airfoil stagnation line [39,51,55]. Compared to those over the hydrophilic airfoil surface, some interesting features can be observed for the ice accretion process over the icephobic airfoil surface. Instead of coalescing rapidly to form a thin water film over the hydrophilic airfoil surface, the supercooled water droplets were found to merge rapidly to form larger water droplets upon impinging onto the icephobic airfoil surface, due to the hydrophobic nature of the surface (i.e., $\theta_{static} \approx 100°$). As a result, the impinged water collected over the airfoil frontal surface (i.e., within the direct impinging zone of the airborne water droplets) was found to run back as isolated water droplets, instead of forming a smooth runback water film/rivulet flow. Corresponding to the smaller capillary forces to restrain the water droplets from running back over the icephobic surface (i.e., ~10% smaller than those on the hydrophilic surface), the unfrozen water droplets were found to travel slightly faster over the icephobic airfoil surface as driven by the same incoming airflow, causing the formation of isolated, droplet-shaped runback ice structures at further downstream locations, as shown clearly in Fig. 3b. With more supercooled water droplets impinged onto the icephobic airfoil surface, the ice structures accreted near the airfoil leading edge were found to grow gradually to form a transparent, glazy ice layer with a rougher surface, i.e., featured by the generation of isolated ice humps, as shown in Fig. 4b. It should also be noted that even though the ice adhesion strength on the icephobic surface is much smaller (i.e., approx. only 15%) than that on the hydrophilic surface, some droplet-shaped runback ice structures were still found to stick firmly to the rear surface of the airfoil model due to the insufficient aerodynamic shear forces in the regions to blow away the small droplet-shaped ice structures accreted on the icephobic airfoil surface, as shown clearly in Fig. 3b.

The acquired images given in Fig. 4c reveal clearly that upon impinging of the supercooled water droplets onto the SHS-coated airfoil surface, ice structures were still found to accrete in the narrow region near the airfoil leading edge due to the vanished aerodynamic shear stress near the airfoil stagnation line. No runback water or ice structures were observed over the rest of the airfoil surface. It can be explained by the fact that, in comparison to that over the hydrophilic or icephobic airfoil surface, the impinged water droplets, except those at the stagnation point, would be much more readily to splash, bounce off, and roll away from the SHS-coated surface due to its outstanding water repellency [51], resulting in much less impinged water droplets remaining on the SHS-coated airfoil surface. Corresponding to its superhydrophobic nature (i.e., $\theta_{static} \approx 153°$), the unfrozen water remaining on the SHS-coated airfoil surface was found to be in the form of isolated water droplets with their size smaller than those on the icephobic surface. Meanwhile, the much smaller capillary force to restrain the unfrozen water droplets from running back over the SHS-coated airfoil surface (i.e., only ~4% of that on the hydrophilic surface) would facilitate the incoming airflow to blow all the tiny water droplets away from the SHS-coated airfoil surface before being frozen into ice. Therefore, no obvious runback of the unfrozen water and ice accretion was observed over the SHS-coated airfoil surface except within the narrow near the airfoil stagnation line (i.e., airflow leading edge). It was also clearly revealed that, with more supercooled water droplets impinging onto the SHS-coated airfoil surface, while the thickness of the ice layer accreted along the airfoil leading edge was found to increase continuously, the coverage of the ice layer was also found to spread gradually to further downstream locations as the time increased.

It should also be noted that the ice layer accreted at the leading edge of SHS-coated airfoil surface was found to be thicker than those at the leading edges of the icephobic and hydrophilic airfoil surfaces after experiencing the same icing experiments (i.e., at $t = 120$ s as shown clearly in Fig. 3b). This is believed to result from the significant differences in the surface wettability for the compared surfaces. As described above, upon the impingement of the same amount of airborne water droplets at the airfoil leading edge, while the impinged droplets would merge rapidly to generate a thin water film over the hydrophilic airfoil surface, isolated water droplets were found to form on the SHS-coated airfoil surface due to its superhydrophobic nature. With the angle of the attack (i.e., AoA) of the airfoil model being zero in the present study, the airfoil leading edge would be the stagnation line of the airflow. Due to the vanished aerodynamic shear forces at the stagnation line, the water droplets at the leading edge of the SHS-coated airfoil were able to remain stationary during the icing experiment and were frozen into ice eventually. Corresponding to the greater heights of the water droplets remaining at the leading edge of the SHS-coated airfoil surface in comparison to those on the icephobic and hydrophilic surfaces as shown in Fig. 2, the ice layer accreted at the leading edge of SHS-coated airfoil surface was found to be thicker than those accreted on the icephobic and hydrophilic surfaces, as shown in Fig. 3b.

B. Comparison of the Hybrid Anti-/De-Icing Systems with Different Surface Coatings

The effects of the surface coatings on the performance of the hybrid anti-/de-icing system were also evaluated systematically in the present study. For the anti-/de-icing experiments, the model airfoil was exposed to the same glaze icing conditions with $V_\infty = 40$ m/s, $T_\infty = -5.0°C$, and LWC $= 2.0$ g/m^3. The film heater wrapped around the airfoil leading edge was turned on first for 70 s before switching on the water spray system of ISU-IRT. Figure 5 shows the snapshot images acquired at two different time instants after turning on the water spray system to reveal the features of the anti-/de-icing operation. Further details of the anti-/de-icing characteristics were revealed more clearly from the zoom-in view near the airfoil leading edge given in Fig. 6. It should be noted that, for the measurement results given in Figs. 5 and 6, the supplied power density for the surface heating was estimated to be $P = 8.3$ kW/m^2 based on the electric power supplied to the film heater wrapped around the airfoil leading edge.

As revealed clearly in Fig. 5, upon switching the electric film heater wrapped around the airfoil leading edge, supercooled water droplets would be heated up rapidly upon impinging onto the heated airfoil frontal surface (i.e., up to the first 10% of the airfoil chord length). With the supplied power density at $P = 8.3$ kW/m^2, the surface heating was found to be sufficient to keep all the impinged water droplets in the liquid phase over the airfoil frontal surface regardless of the surface wettability, indicating that the surface heating is effective to prevent ice accretion along the airfoil stagnation line. Driven by the aerodynamic shear forces exerted by the incoming

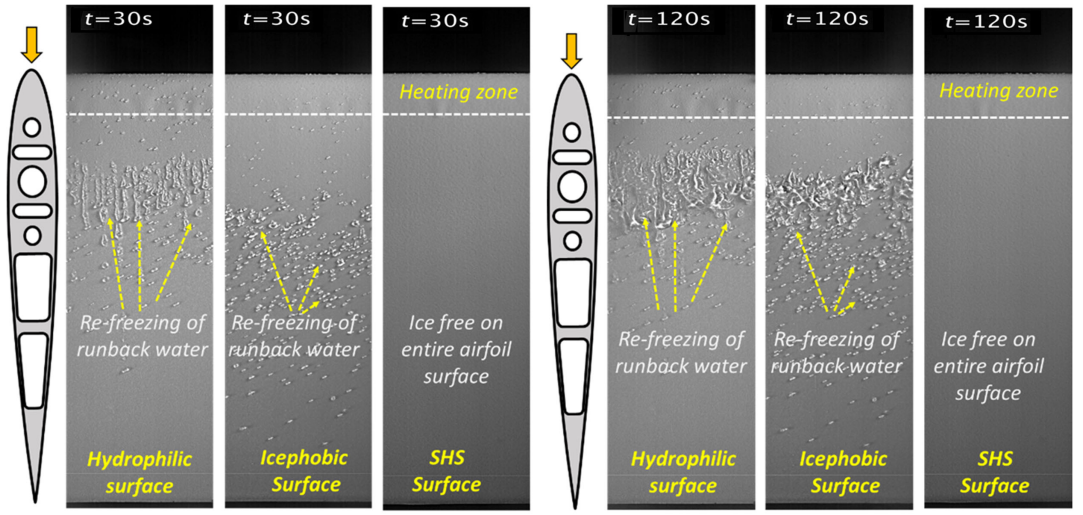

a) Acquired images at $t = 30$ s b) Acquired images at $t = 120$ s

Fig. 5 Snapshot images reveal the features of the anti-/de-icing operation with the supplied power density for surface heating at $P = 8.3$ kW/m^2.

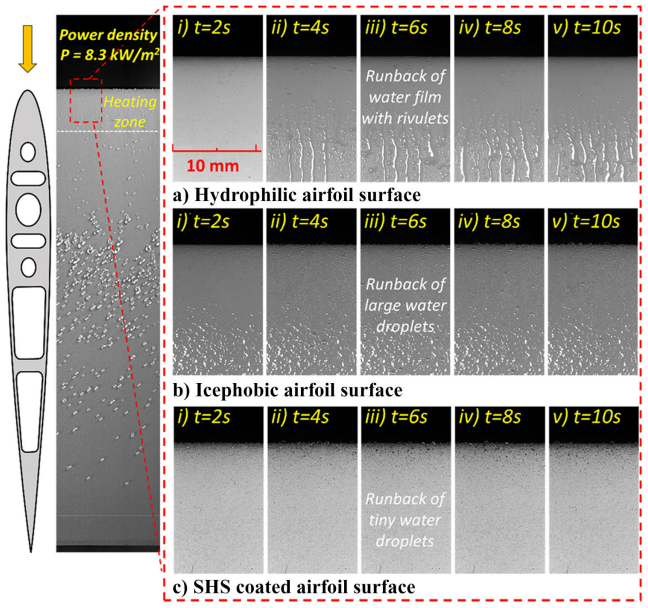

Fig. 6 Zoom-in views of the anti-/de-icing process near the airfoil leading edge.

airflow, the impinged water collected over the airfoil front surface (i.e., within the direct impinging zone of the airborne water droplets) was found to run back toward the airfoil trailing edge, transporting the impinged water mass from the airfoil frontal surface to further downstream locations.

As shown clearly in Fig. 6a, due to the hydrophilic nature of the enamel-coated airfoil surface, the impinged water droplets were found to coalesce rapidly to form a thin water film flow with multiple rivulets over the hydrophilic airfoil surface, transporting the impinged water collected near the airflow leading edge to further downstream regions. Since the temperature of the incoming airflow was maintained at frozen cold during the experiment (i.e., $T_\infty = -5.0$°C), the runback water film/rivulet flow was cooled down gradually as the water moved out of the heating zone (i.e., the area protected by the electric film heater). Once the temperature of the runback water became lower than the water freezing temperature, the runback water would be frozen into ice, causing the formation of the rivulet-shaped runback ice structures at the further downstream locations (i.e., beyond the first 20% of the airfoil chord length at $t = 30$ s, as revealed clearly in Fig. 5). In summary, even with the airfoil surface being hydrophilic, the active method with sufficiently electric power supplied for the surface heating (e.g., at $P = 8.3$ kW/m^2) was demonstrated to be effective to eliminate ice accretion over the airfoil frontal surface. However, the surface heating method could not keep the entire airfoil surface ice-free due to the refreezing of the runback water in the downstream regions (i.e., beyond the area protected by the film heater). A much higher power density would be required (i.e., up to $P \approx 45$ kW/m^2) for the surface heating in order to keep the entire hydrophilic airfoil surface ice-free, which will be discussed further in the next section.

As revealed clearly in Fig. 6b, with the airfoil surface covered with the icephobic coating, the surface heating method was also found to be very effective in eliminating ice accretion over the airfoil frontal surface. As described above, the impinged water droplets collected over the airfoil frontal surface were found to merge into larger water droplets on the icephobic airfoil surface due to its hydrophobic nature (i.e., $\theta_{static} \approx 100°$). As a result, the impinged water was found to run back as isolated moving water droplets over the icephobic airfoil surface, causing the formation of droplet-shaped ice structures over the rear surface of the model airfoil, as shown clearly in Fig. 5. It can also be seen that since the capillary forces to restrain the running back water droplets on the icephobic surface are smaller than those on the hydrophilic surface (i.e., ~10% smaller), the runback water droplets would be able to move slightly faster over the icephobic airfoil surface, thereby reaching further downstream locations before being frozen into ice (i.e., reaching $X/C > 30\%$ at $t = 30$ s as revealed clearly in Fig. 5). In summary, the hybrid method with the power density supplied for the surface heating being $P = 8.3$ kW/m^2, the icephobic coating was proven to be unsuccessful in preventing ice accretion on the entire airfoil surface under the glaze icing conditions of the present study.

As shown clearly in Fig. 5, the hybrid system with the SHS-coated airfoil surface was found to be very effective for the anti-/de-icing operation. With the supplied power density for surface heating at $P = 8.3$ kW/m^2, the entire airfoil surface was found to be completely ice-free during the entire anti-/de-icing experiment. This is believed to be due to the following reasons:

1) Due to its extraordinary water repellency, the impinged supercooled water droplets (except those at the airfoil leading edge) would be more readily to splash, bounce and roll off from the SHS-coated airfoil surface, resulting in much less amount of the water mass remaining on the SHS-coated airfoil surface for possible ice formation, as shown clearly in Fig. 6c.

2) The extreme small capillary force to restrain water droplets from running back on the SHS-coated airfoil surface (i.e., only ~4% of that on the hydrophilic surface) would also facilitate the incoming airflow to blow the water droplets away from the SHS-coated airfoil surface before freezing into ice.

C. IR Thermal Imaging Results to Quantify the Anti-/De-Icing Process

The effects of the surface coatings on the characteristics of the anti-/de-icing operation over the airfoil surface were revealed more clearly and quantitatively from the IR thermal imaging measurements. Figure 7 shows typical IR imaging results to characterize the temperature distributions over the airfoil surfaces with the power density supplied for the surface heating at $P = 8.3$ kW/m^2. The time evolution profiles of the spanwise-averaged surface temperatures at four chordwise locations over the airfoil surface, i.e., near the airfoil leading edge at $X/C \approx 0.5\%$, at the middle of the heating zone at $X/C \approx 4.0\%$, near the end of the heating zone at $X/C \approx 8.0\%$, and downstream of the heating zone at $X/C \approx 16\%$, are also given in Fig. 7 for a quantitative comparison.

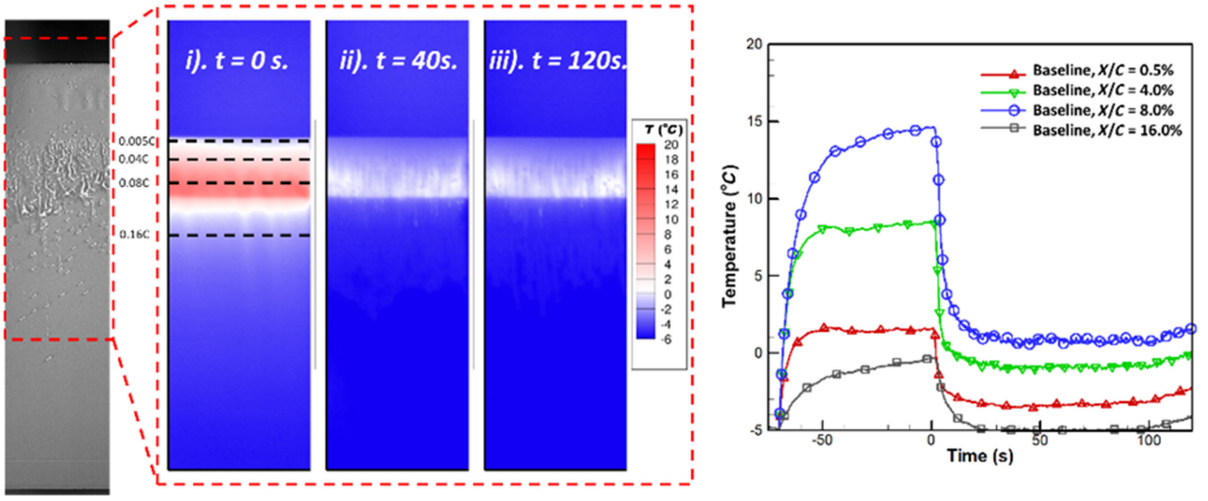

a) Measured temperature over the hydrophilic airfoil surface (baseline)

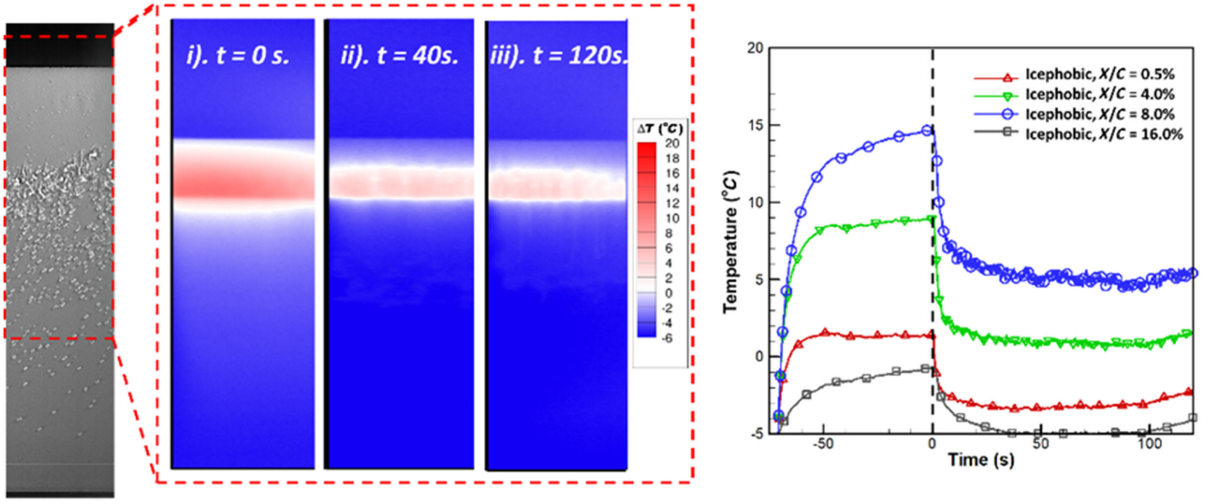

b) Measured temperature over the icephobic airfoil surface

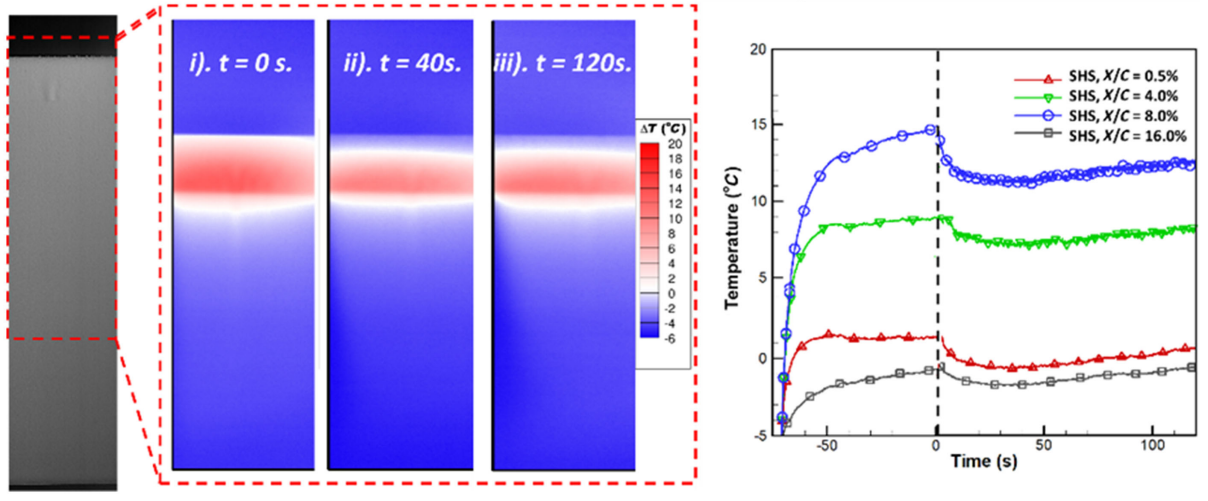

c) Measured temperature over the SHS coated airfoil surface

Fig. 7 Time evolutions of airfoil surface temperature during the anti-/de-icing operation.

As revealed quantitatively from the IR thermal imaging results given in Fig. 7, the surface temperature distributions over the airfoil surface were found to have very similar characteristics in general, regardless of surface coating used to coat the model airfoil. Once the film heater was turned on, the temperature over the airfoil frontal surface (i.e., the area protected by the film heater) was found to increase monotonically at first, then flat out gradually as the system reached a thermally stable state. With the supplied power density for surface heating being $P = 8.3$ kW/m^2, while the temperature of the incoming airflow was set at $T_\infty = -5.0$°C, the temperature at the rear portion of the heating zone was found to be well above the water freezing temperature (e.g., $T_w \approx +15$°C at $X/C \approx 8.0\%$) right before switching on the water spray system (i.e., at $t = 0$ s). The surface temperature near the airfoil leading edge was much lower (e.g., $T_w \approx +2.0$°C at $X/C \approx 0.5\%$) due to the much stronger convective heat transfer in the region near the airfoil leading edge [77]. The surface temperature in the downstream region beyond the heating zone (e.g., at $X/C \approx 0.16$) was also found to increase slightly due to the thermal flux from the upstream heating zone via both conductive and convective heat transfer.

After switching on the water spray system of the ISU-IRT at $t = 0$ s, the surface temperature near the airfoil leading edge was found to drop sharply at first, upon the impingement of airborne supercooled water droplets onto the airfoil frontal surface. Then, the surface temperature in the heating zone was found to decrease at a moderate rate and flattened gradually at the time of $t > 40$ s. A slight increase in the measured temperature was also observed at the later stage of the experiment (i.e., $t > 50$ s). This is believed to be caused by the energy deposition associated with the continuous energy addition to the test model for the surface heating (i.e., the test model was heated up gradually as the time progresses).

More interesting features can be identified by carefully comparing the time evolution characteristics of the measured temperatures on the airfoil surfaces coated with different coatings. As revealed clearly from the measured results given in Fig. 7a, upon the impingement of supercooled water droplets onto the hydrophilic airfoil surface, the surface temperature near the airfoil leading edge was found to become lower than the water freezing temperature quickly (i.e., $T_w < -3.0$°C at $X/C \approx 0.5\%$ at $t > 10$ s). As shown clearly from the acquired images given in Fig. 6a, since no ice structures were found to accrete near the airfoil leading edge, the impinged water would still stay in a supercooled state near the airfoil leading edge due to the limited surface heating for this test case (i.e., $P \approx 8.3$ kW/m^2). Driven by the aerodynamic shear forces exerted by the incoming airflow, the unfrozen water collected over the airfoil frontal surface would run back to approach the trailing edge, forming a runback water film with multiple rivulets along its moving front contact line. The runback water film/rivulet flow would be heated continuously to increase its temperature until flowing out of the heating zone (i.e., the measured temperature was found to increase to $T_w \approx +2.0$°C at $X/C \approx 8.0\%$). However, since the airflow over the airfoil surface was frozen-cold (i.e., $T_\infty = -5$°C), the runback water would be cooled down gradually as flowing out of the heating zone (i.e., in the downstream region of $X/C > 10\%$). As shown quantitatively in Fig. 7a, the temperature of the runback water at the downstream location of $X/C \approx 16\%$ was found to become almost the same as the frozen-cold incoming airflow (i.e., $T_w = -5.0$°C) within 20 s after switching on the water spray system (i.e., at $t > 20$ s). As a result, the runback water was found to be refrozen into runback ice at further downstream locations (i.e., starting at $X/C \approx 20\%$ at $t = 30$ s as revealed clearly in the acquired images given in Fig. 5).

As revealed quantitatively in Fig. 7b, while the time evolution characteristics of the measured surface temperatures on the icephobic airfoil surface were found to be very similar as those on the hydrophilic surface, some subtle differences can still be identified from the measurement results given in Fig. 7b. As aforementioned, in comparison to that on the hydrophilic surface, impinging water droplets would be more readily to bounce off and splash from the icephobic airfoil surface due to its hydrophobic nature (i.e., $\theta_{\text{static}} \approx 100°$), causing less impinged water droplets remaining over the airfoil frontal surface. Therefore, upon the impingement of same amount of airborne supercooled water droplets, the temperature in the region near the airfoil leading edge (e.g., at $X/C \approx 0.5\%$) was found to be slightly higher (i.e., ~0.5°C higher) than that on the hydrophilic airfoil surface. With the same supplied power density of $P \approx 8.3$ kW/m^2 for surface heating, less water collected over the airfoil frontal surface was found to cause higher surface temperatures within the heating zone on the icephobic airfoil surface (i.e., about ~4.7°C higher at $X/C \approx 8.0\%$) than that on the hydrophilic surface. More specifically, with the system reaching the thermally stable state at $t > 40$ s, the measured temperature at the end of the heating zone (e.g., at $X/C \approx 8.0\%$) on the icephobic airfoil surface was measured to be $T_w \approx +5.4$°C, the corresponding value was found to be only $T_w \approx +0.70$°C on the hydrophilic surface. Since the incoming airflow was kept as frozen cold during the experiment (i.e., $T_\infty = -5.0$°C), the runback water would be cooled down rapidly once flowing out of the heating zone. Because the runback water had a higher temperature at the end of the heating zone on the icephobic airfoil surface, the runback water would be able to travel for a longer distance (i.e., reaching further downstream locations on the icephobic airfoil surface) before being frozen into ice, in comparison to that on the hydrophilic airfoil surface, as revealed clearly from the snapshot images given in Fig. 6.

With the supplied power density for surface heating at the same level of $P = 8.3$ kW/m^2, the measured surface temperatures on the SHS-coated airfoil surface were found to be much higher than those of the other two cases. More specifically, after switching on the water spray system for 40 s (i.e., at $t = 40$ s), while the surface temperature near the airfoil leading edge (i.e., at $X/C \approx 0.5\%$) was found to increase to $T_w \approx -0.50$°C (i.e., ~3.0°C higher than that on the hydrophilic surface), the corresponding value at the end of the heated zone (e.g., at $X/C \approx 8.0\%$) was measured to be $T_w \approx +11.6$°C (i.e., ~11.0°C higher than those on the hydrophilic surface), which was well above the water freezing temperature. This can be explained by the fact that, due to the extraordinary water repellency of the SHS-coated surface, a significant portion of the impinging supercooled water droplets would bounce off from the SHS-coated airfoil surface [51], except those in the region near the airfoil leading edge (i.e., the stagnation line). This would result in much less water mass remaining on the airfoil surface. As shown clearly in Fig. 6c, since much fewer impinged droplets would be collected on the SHS-coated airfoil surface, a much smaller portion of the supplied energy will be dissipated for heating the impinged supercooled water droplets, leading to the much higher surface temperature within the heating zone on the SHS-coated airfoil surface. As a result, the surface temperature in the downstream region beyond the heating zone was also found to become higher on the SHS-coated surface (e.g., $T_w \approx -1.69$°C at $X/C \approx 16\%$) than that on hydrophilic surface (i.e., $T_w \approx -5.0$°C at the same downstream location). In addition to having much higher temperature to delay the ice accretion process, the extreme small capillary forces to restrain the water droplets from running back over the SHS-coated surface (i.e., only ~4% of that on the hydrophilic surface) would also facilitate the incoming airflow to blow away the tiny water droplets from the SHS-coated airfoil surface. Therefore, with the same supplied power density of $P = 8.3$ kW/m^2 for the anti-/de-icing operation, the SHS-coated airfoil surface was found to be completely ice-free, as shown clearly in the snapshot image given in Fig. 5c.

D. Determination of the Minimized Electric Power Input Required for Anti-/De-Icing Operation

As described above, with the same supplied power density of $P = 8.3$ kW/m^2 for the anti-/de-icing operation, while the SHS-coated airfoil surface was found to be completely ice-free, substantial ice structures were still found to accrete over the hydrophilic and icephobic airfoil surfaces due to the refreezing of the runback water in the downstream region beyond the area protected by the film heater. It was found that the hydrophilic and icephobic airfoil surfaces could also become ice-free if higher electric powers were supplied to the film heater wrapped around the airfoil leading edge.

In the present study, a parametric study was conducted to determine the minimum power input required by the film heater for a successful anti-/de-icing operation (i.e., to keep the entire airfoil surface ice-free) for the three compared coatings. During the experiments, while the model airfoil was exposed to the same glaze icing conditions (i.e., $V_\infty = 40$ m/s, LWC $= 2.0$ g/m^3, and $T_\infty = -5$°C), the electric power supplied to the film heater was increased gradually until the entire airfoil surface became ice-free during the entire anti-/de-icing experiment (i.e., up to 180 s after switching on the water spray system of ISU-IRT).

Figure 8 shows typical snapshot images of the airfoil surfaces treated with different surface coatings when the electric power supplied to the film heater was increased gradually for the anti-/de-icing operation. The images were acquired at $t = 120$ s (i.e., 120 s later after switching on the water spray system). As shown clearly in Fig. 8a, when the electric power supplied for the surface heating was relatively lower (i.e., $P \approx 8.3$ kW/m^2), while the active anti-/de-icing method of heating the airfoil frontal surface was found to be effective in preventing ice accretion near the airfoil leading edge, substantial rivulet-shaped runback ice structures were observed to accrete over the hydrophilic airfoil surface in the downstream region of $X/C > 17\%$. When the supplied power density for surface heating increased to $P \approx 25$ kW/m^2, since the runback water would be heated up more intensively as flowing over the heating zone, it would delay the freezing process of the runback water in the downstream region. As a result, no rivulet-shaped runback ice structures were found to accrete over the hydrophilic airfoil surface up to the downstream region of $X/C > 56\%$. When the supplied power density was further increased to $P \approx 45$ kW/m^2, all the impinged water collected over the airfoil frontal surface was found to be able to stay in liquid form during the entire runback process over the hydrophilic airfoil surface, which would shed off from the airfoil leading edge eventually. As a result, no ice structures were found to accrete over the entire hydrophilic airfoil surface, as revealed clearly in Fig. 8a.

A very similar scenario was also observed over the icephobic airfoil surface as the power supplied to the film heater increased gradually for the anti-/de-icing operation. Since less impinged supercooled water droplets would be able to remain over the icephobic airfoil surface because of its hydrophobic nature, the ice-free zone over the airfoil frontal surface was found to be extended to further downstream locations, in comparison to those over the hydrophilic airfoil surface. With the same supplied power density of $P \approx 25$ kW/m^2, droplet-shaped runback ice structures were found to accrete in the downstream region of $X/C > 67\%$ over the icephobic airfoil surface, as shown clearly in Fig. 8b. When the supplied power density was further increased to $P \approx 40$ W/m^2, while the impinged water droplets collected over the airfoil frontal surface were found to be heated up so much that they were able to stay in liquid phase during the entire runback process; therefore, no ice was found to accrete over the entire icephobic airfoil surface.

As revealed clearly in Fig. 8c, a much lower electric power is required for the hybrid anti-/de-icing system to prevent ice accretion over the SHS-coated airfoil surface. No ice was found to accrete over the entire SHS-coated airfoil surface once the power density supplied for the surface heating became greater than $P \approx 4.6$ kW/m^2, which is only 10% of that required for the case with the airfoil surface covered with the hydrophilic coating.

Table 2 summarizes the minimum power density required for a successful anti-/de-icing operation (i.e., to keep the entire airfoil surfaces ice-free). It can be seen clearly that, in comparison to the active approach of forceful heating the hydrophilic airfoil surface, the hybrid anti-/de-icing system with the icephobic and SHS coatings would achieve a power saving of 10 and 90% under the same glaze icing condition, respectively. It also suggests that, compared with the icephobicity, the surface wettability will play a much more dominant role in reducing the power consumption required for the anti-/de-icing oper-

Table 2 Minimum power density required to keep entire airfoil surface ice-free

Compared surface coating	Required minimum power density for the anti-/de-icing operation, kW/m^2	Power saving for the anti-/de-icing, %
Hydrophilic coating	45	— —
Icephobic coating	40	~12
SHS coating	4.6	~90

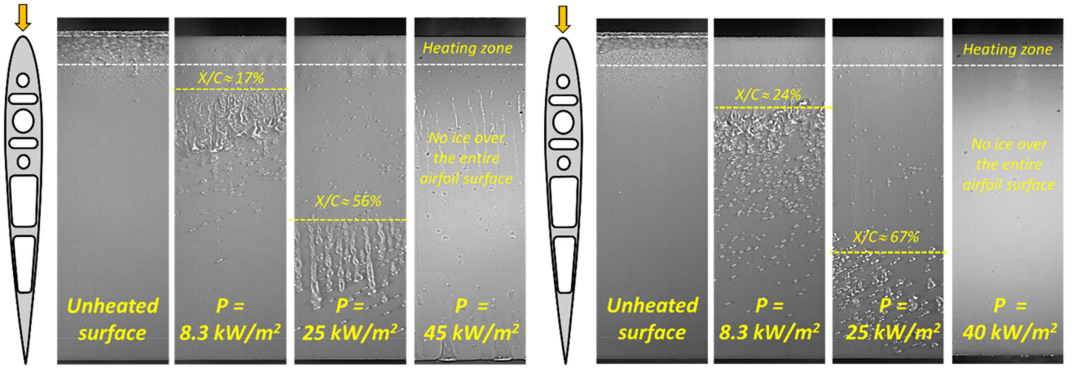

a) Over the hydrophilic airfoil surface at t =120s

b) Over the icephobic airfoil surface at t =120s

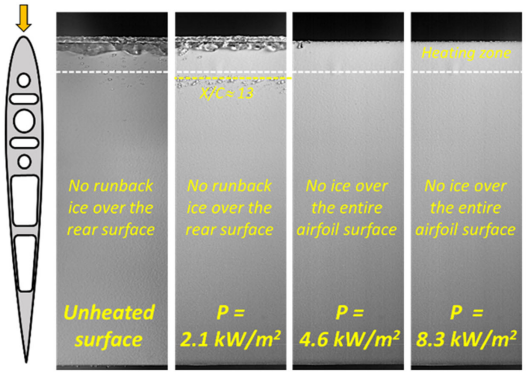

c) On the SHS-coated airfoil surface at t =120s

Fig. 8 The acquired images with different power density levels supplied for surface heating.

ation. As described above, due to its extraordinary water repellency, the SHS-coated airfoil surface would reject most of the impinging supercooled water droplets from staying on the SHS-coated airfoil surface effectively, which would significantly reduce the ice accretion on the airfoil surface. Meanwhile, the much smaller capillary force to restrain the water droplets from running back will enable the water droplet to move more freely over the SHS-coated airfoil surface, facilitating the airflow to blow the water droplets away from the SHS-coated airfoil surface, instead of forming runback ice structures.

Even though the ice adhesion strength on the icephobic airfoil surface is significantly less than that on the hydrophilic airfoil surface (i.e., ~90% smaller), the capillary forces acting on the runback water droplets were found to be only slightly smaller than those on the hydrophilic airfoil surface (i.e., only ~10% smaller). As a result, the impinged water collected over the airfoil frontal surface would run back gradually over the icephobic airfoil surface. Interacting with the frozen cold airflow above the airfoil surface, the runback water would be cooled down continuously once flowing out of the heating zone (i.e., the area protected by the film heater) and was found to refreeze into ice eventually at further downstream locations. Despite the relatively small ice adhesion strength to the icephobic surface (i.e., $\tau_{ice} \approx 75$ kPa), the aerodynamic shear forces exerted by the boundary-layer airflow over the airfoil rear surface were still too weak to remove the accreted ice structures from the icephobic airfoil surfaces. As a result, a substantially high-power density would be required to heat the runback water to enable them to stay in liquid phase until shedding off from the airfoil trailing edge. In summary, in comparison to the baseline case of forceful heating the hydrophilic airfoil surface, while the hybrid anti-/de-icing system with the SHS-coated airfoil surface would achieve about 90% energy savings in preventing ice accretion over the entire airfoil surface, the hybrid system with the icephobic coating could only reduce the energy consumption required for the anti-/de-icing operation by 10%.

IV. Conclusions

An experimental study was conducted to examine the effects of surface wettability and icephobicity on the performance of a hybrid anti-/de-icing approach that combines surface heating near the airfoil leading edge with either hydrophobic or icephobic surface coatings for aircraft icing mitigation. The experimental study was conducted in an Icing Research Tunnel of Iowa State University (ISU-IRT) with an airfoil/wing model exposed to typical glazy icing conditions. While the airfoil model was wrapped with a flexible electric film heater around its leading edge to actively prevent ice accretion on the airfoil frontal surface, three kinds of surface coatings with different hydrophilicity and icephobicity were applied to coat the airfoil surface in three distinct segments along the model span. The compared coatings included 1) an icephobic coating with very small ice adhesion strength and weak hydrophobicity, 2) an SHS coating with outstanding water repellency but a moderate icephobicity, and 3) a commonly used protective hydrophilic coating with a relatively poor hydrophobicity and strong ice adhesion strength as the baseline for the comparative study. During the experiment, in addition to using high-speed imaging systems to record the dynamic icing and anti-/de-icing process over the airfoil surfaces coated with different coatings, a high-speed IR thermal imaging system was also used to characterize the unsteady heat transfer process over the airfoil surfaces.

The characteristics of the dynamic ice accretion process over the airfoil surface were found to be affected by the surface wettability significantly. In comparison to those on the hydrophilic airfoil surface (i.e., the baseline case), impinging supercooled water droplets would be more readily to rebound and roll off from the icephobic airfoil surface due to its hydrophobic nature, resulting in less impinged water droplets remaining on the icephobic airfoil surface. Instead of forming a water film/rivulet flow as that on the hydrophilic airfoil surface, the impinged water droplets were found to merge quickly into larger droplets and run back toward the airfoil trailing edge as isolated droplets on the icephobic airfoil surface. Corresponding to the smaller capillary forces to restrain the water droplets from moving on the icephobic surface, the runback water droplets were found to be able to travel farther distances approaching the airfoil trailing edge before being frozen into ice. It resulted in the formation of the droplet-shaped ice structures at further downstream locations on the icephobic airfoil surface. Because of its superhydrophobicity, much more impinging supercooled water droplets were found to rebound and roll off quickly from the SHS-coated airfoil surface, resulting in less ice accreting over the airfoil frontal surface. Thanks to its extraordinary water repellency, the impinged water droplets were much more readily blown away by the incoming airflow from the SHS-coated airfoil surface, resulting in no runback ice accreted on the SHS-coated airfoil surface.

After the electric film heater wrapped around the airfoil leading edge was turned on, the impinged supercooled water droplets were found to be heated up rapidly and stay in liquid phase over the airfoil frontal surface, thereby eliminating ice accretion near the airfoil leading edge regardless of the applied coatings. The impinged water would run back over the airfoil surface as driven by the incoming airflow. Interacting with the frozen cold airflow over the airfoil surface, the runback surface water was cooled down continuously once flowing out of the heating zone (i.e., the area protected by the film heater), leading to refreezing of the runback water into runback ice at further downstream locations. As the electric power supplied to the film heater increased, the occurrence of the runback ice accretion was found to be pushed further downstream locations, approaching the airfoil trailing edge. With the electric power supplied for surface heating becoming high enough, the runback water was found to be able to stay in liquid phase during the entire runback process and shed off eventually from the airfoil trailing edge, resulting in no ice accretion over the entire airfoil surface.

The minimum electric power required for surface heating to achieve a successful anti/de-icing operation (i.e., making the entire airfoil surface ice-free) was found to be highly dependent on the wettability of the airfoil surface. In comparison to the baseline case of forceful heating the hydrophilic airfoil surface, the hybrid anti-/de-icing approach with SHS coating was found to achieve about 90% energy savings in preventing ice accretion over the entire airfoil surface, thanks to its extraordinary water repellency. Because of its weak hydrophobicity, the hybrid system with the icephobic coating was found to reduce the energy consumption required for the anti-/de-icing operation by only about 10%, despite its outstanding icephobicity. The research findings suggest that the wettability of the airfoil surface would play a much more dominant role than the icephobicity in affecting the performance of a hybrid ant-/de-icing system for aircraft icing mitigation.

It should also be noted that, since the primary objective of the present study is to explore novel anti-/de-icing strategies for the icing protection of modern aircraft and UAVs, the experimental study was conducted with an airfoil model made of polymer-based material with relatively low thermal conductivity. While the research findings derived from the present study are believed to be also applicable to traditional metal-based aircraft in general, the effects of the significant difference in the thermal conductivity between the conventional metal-based aircraft (i.e., ~200 $W/[m \cdot K]$) and the polymer-based modern aircraft (i.e., ~0.2 $W/[m \cdot K]$) on the icing characteristics and anti-/de-icing operation should be considered carefully, which will be investigated systematically in a future study.

Acknowledgments

The research work is partially supported by the National Science Foundation under award numbers CBET-1916380, CBET-1935363, and CBET-2313310. The authors want to thank Yang Liu, Nianhong Han, James Benson, and Andrew Jordan of Iowa State University (ISU) for their help in operating the ISU's icing research tunnel facilities.

References

[1] Ueno, K., and Farzaneh, M., "Linear Stability Analysis of Ice Growth Under Supercooled Water Film Driven by a Laminar Airflow," *Physics of Fluids*, Vol. 23, No. 4, 2011, Paper 042103. https://doi.org/10.1063/1.3575605

[2] Fortin, G., Laforte, J. L., and Ilinca, A., "Heat and Mass Transfer During Ice Accretion on Aircraft Wings with an Improved Roughness Model," *International Journal of Thermal Sciences*, Vol. 45, No. 6, 2006, pp. 595–606. https://doi.org/10.1016/j.ijthermalsci.2005.07.006

[3] Liu, Y., Bond, L. J., and Hu, H., "Ultrasonic-Attenuation-Based Technique for Ice Characterization Pertinent to Aircraft Icing Phenomena," *AIAA Journal*, Vol. 55, No. 5, 2017, pp. 1–8. https://doi.org/10.2514/1.J055500

[4] Liu, Y., Li, L., Ning, Z., Tian, W., and Hu, H., "Experimental Investigation on the Dynamic Icing Process over a Rotating Propeller Model," *Journal of Power and Propulsion*, Vol. 34, No. 4, 2018, pp. 1–15. https://doi.org/10.2514/1.B36748

[5] Hu, H., Tian, L., and Hu, H., "Experimental Investigation on Ice Accretion Upon Ice Particle Impacting onto Heated Surface," *AIAA Journal*, Vol. 61, No. 7, 2023, pp. 1–13. https://doi.org/10.2514/1.J062425

[6] Hu, H., Al-Masri, F., Tian, L., and Hu, H., "Experimental Study of Dynamic Icing Process on a Pitot Probe Model," *Journal of Thermophysics and Heat Transfer*, Vol. 37, No. 3, 2023, pp. 1–12. https://doi.org/10.2514/1.T6782

[7] Cao, Y., Tan, W., and Wu, Z., "Aircraft Icing: An Ongoing Threat to Aviation Safety," *Aerospace Science and Technology*, Vol. 75, April 2018, pp. 353–385. https://doi.org/10.1016/j.ast.2017.12.028

[8] Bragg, M. B., Gregorek, G. M., and Lee, J. D., "Airfoil Aerodynamics in Icing Conditions," *Journal of Aircraft*, Vol. 23, No. 1, 1986, pp. 76–81. https://doi.org/10.2514/3.45269

[9] Vasquez, T., "Air France Flight 447: A Detailed Meteorological Analysis," *Weather Graphics*, 2009, http://scholar.google.com/scholar?q=Air+France+Flight+447+&btnG=&hl=en&as_sdt=0%2C16#5 [retrieved 1 Oct. 2015].

[10] Liu, Y., Ma, L., Wang, W., Kota, A. K., and Hu, H., "An Experimental Study on Soft PDMS Materials for Aircraft Icing Mitigation," *Applied Surface Science*, Vol. 447, July 2018, pp. 599–609. https://doi.org/10.1016/j.apsusc.2018.04.032

[11] Kent, R. A., Andersen, D., Caux, P. Y., and Teed, S., "Canadian Water Quality Guidelines for Glycols—An Ecotoxicological Review of Glycols and Associated Aircraft Anti-Icing and Deicing Fluids," *Environmental Toxicology*, Vol. 14, No. 5, 1999, pp. 481–522. https://doi.org/10.1002/(SICI)1522-7278(199912)14:5<481::AID-TOX5>3.0.CO;2-8

[12] Thomas, S. K., Cassoni, R. P., and MacArthur, C. D., "Aircraft Anti-Icing and De-Icing Techniques and Modeling," *Journal of Aircraft*, Vol. 33, No. 5, 1996, pp. 841–854. https://doi.org/10.2514/3.47027

[13] Ramakrishna, D. M., and Viraraghavan, T., "Environmental Impact of Chemical Deicers–A Review," *Water, Air, & Soil Pollution*, Vol. 166, No. 49, 2005, pp. 1–7. https://doi.org/10.1007/s11270-005-8265-9

[14] Overmeyer, A., Palacios, J., and Smith, E., "Ultrasonic De-Icing Bondline Design and Rotor Ice Testing," *AIAA Journal*, Vol. 51, No. 12, 2013, pp. 2965–2976. https://doi.org/10.2514/1.J052601

[15] Parent, O., and Ilinca, A., "Anti-Icing and De-Icing Techniques for Wind Turbines: Critical Review," *Cold Regions Science and Technology*, Vol. 65, No. 1, 2011, pp. 88–96. https://doi.org/10.1016/j.coldregions.2010.01.005

[16] Liu, Y., Kolbakir, C., Hu, H., and Hu, H., "A Comparison Study on the Thermal Effects in DBD Plasma Actuation and Electrical Heating for Aircraft Icing Mitigation," *International Journal of Heat and Mass Transfer*, Vol. 124, Sept. 2018, pp. 319–330. https://doi.org/10.1016/J.IJHEATMASSTRANSFER.2018.03.076

[17] Li, L., Liu, Y., Tian, L., Hu, H., Hu, H., Liu, X., Hogate, I., and Kohli, A., "An Experimental Study on a Hot-Air-Based Anti-/De-Icing System for Aero-Engine Inlet Guide Vanes," *Applied Thermal Engineering*, Vol. 167, Feb. 2020, Paper 114778. https://doi.org/10.1016/j.applthermaleng.2019.114778

[18] Kolbakir, C., Hu, H., Liu, Y., and Hu, H., "An Experimental Study on Different Plasma Actuator Layouts for Aircraft Icing Mitigation," *Aerospace Science and Technology*, Vol. 107, Dec. 2020, Paper 106325. https://doi.org/10.1016/j.ast.2020.106325

[19] Meng, X., Hu, H., Yan, X., Liu, F., and Luo, S., "Lift Improvements Using Duty-Cycled Plasma Actuation at Low Reynolds Numbers," *Aerospace Science and Technology*, Vol. 72, Jan. 2018, pp. 123–133. https://doi.org/10.1016/j.ast.2017.10.038

[20] Chen, J., Liang, H., Wu, Y., Wei, B., Zhao, G., Tian, M., and Xie, L., "Experimental Study on Anti-Icing Performance of NS-DBD Plasma Actuator," *Applied Sciences*, Vol. 8, No. 10, 2018, p. 1889. https://doi.org/10.3390/app8101889

[21] Cheng, Y., Rodak, D., Wong, C., and Hayden, C., "Effects of Micro-and Nano-Structures on the Self-Cleaning Behaviour of Lotus Leaves," *Nanotechnology*, Vol. 17, No. 5, 2006, pp. 1359–1362.

[22] Liu, Q., Wu, K.-T., Kobayashi, M., Jen, C.-K., and Mrad, N., "In-Situ Ice and Structure Thickness Monitoring Using Integrated and Flexible Ultrasonic Transducers," *Smart Materials and Structures*, Vol. 17, No. 4, 2008, pp. 45,021–45,023.

[23] Cao, L., Jones, A. K., Sikka, V. K., Wu, J., and Gao, D., "Anti-Icing Superhydrophobic Coatings," *Langmuir : The ACS Journal of Surfaces and Colloids*, Vol. 25, No. 21, 2009, pp. 12,444–12,448. https://doi.org/10.1021/la902882b

[24] Mishchenko, L., Hatton, B., and Bahadur, V., "Design of Ice-Free Nanostructured Surfaces Based on Repulsion of Impacting Water Droplets," *ACS Nano*, Vol. 4, No. 12, 2010, pp. 7699–7707.

[25] Antonini, C., Villa, F., and Marengo, M., "Oblique Impacts of Water Drops onto Hydrophobic and Superhydrophobic Surfaces: Outcomes, Timing, and Rebound Maps," *Experiments in Fluids*, Vol. 55, No. 4, 2014, p. 1713. https://doi.org/10.1007/s00348-014-1713-9

[26] Meuler, A., McKinley, G., and Cohen, R., "Exploiting Topographical Texture to Impart Icephobicity," *ACS Nano*, Vol. 4, No. 12, 2010, pp. 7048–7052.

[27] Cassie, A., and Baxter, S., "Wettability of Porous Surfaces," *Transactions of the Faraday Society*, Vol. 40, 1944, pp. 546–551.

[28] Wenzel, R., "Resistance of Solid Surface to Wetting by Water," *Industrial & Engineering Chemistry*, Vol. 28, No. 8, 1936, pp. 988–994.

[29] Sarshar, M. A., Swarctz, C., Hunter, S., Simpson, J., and Choi, C.-H., "Effects of Contact Angle Hysteresis on Ice Adhesion and Growth on Superhydrophobic Surfaces Under Dynamic Flow Conditions," *Colloid and Polymer Science*, Vol. 291, No. 2, 2013, pp. 427–435. https://doi.org/10.1007/s00396-012-2753-4

[30] Lv, J., Song, Y., Jiang, L., and Wang, J., "Bio-Inspired Strategies for Anti-Icing.," *ACS Nano*, Vol. 8, No. 4, 2014, pp. 3152–3169. https://doi.org/10.1021/nn406522n

[31] Soltis, J., Palacios, J., Eden, T., and Wolfe, D., "Ice Adhesion Mechanisms of Erosion-Resistant Coatings," *AIAA Journal*, Vol. 53, No. 3, 2015, pp. 654–662. https://doi.org/10.2514/1.J053208

[32] Jung, S., Dorrestijn, M., Raps, D., Das, A., Megaridis, C. M., and Poulikakos, D., "Are Superhydrophobic Surfaces Best for Icephobicity?," *Langmuir*, Vol. 27, No. 6, 2011, pp. 3059–3066. https://doi.org/10.1021/la104762g

[33] Schutzius, T. M., Jung, S., Maitra, T., Eberle, P., Antonini, C., Stamatopoulos, C., and Poulikakos, D., "Physics of Icing and Rational Design of Surfaces with Extraordinary Icephobicity," *Langmuir*, Vol. 31, No. 17, 2015, pp. 4807–4821. https://doi.org/10.1021/la502586a

[34] Menini, R., and Farzaneh, M., "Advanced Icephobic Coatings," *Journal of Adhesion Science and Technology*, Vol. 25, No. 9, 2011, pp. 971–992. https://doi.org/10.1163/016942410X533372

[35] Golovin, K., Kobaku, S. P. R., Lee, D. H., DiLoreto, E. T., Mabry, J. M., and Tuteja, A., "Designing Durable Icephobic Surfaces," *Science Advances*, Vol. 2, No. 3, 2016, Paper e1501496. https://doi.org/10.1126/sciadv.1501496

[36] Irajizad, P., Al-Bayati, A., Eslami, B., Shafquat, T., Nazari, M., Jafari, P., Kashyap, V., Masoudi, A., Araya, D., and Ghasemi, H., "Stress-Localized Durable Icephobic Surfaces," *Materials Horizons*, Vol. 6, No. 4, 2019, pp. 758–766. https://doi.org/10.1039/c8mh01291a

[37] Elzaabalawy, A., and Meguid, S. A., "Advances in the Development of Superhydrophobic and Icephobic Surfaces," *International Journal of Mechanics and Materials in Design*, Vol. 18, No. 3, 2022, pp. 509–547. https://doi.org/10.1007/S10999-022-09593-X

[38] Ma, L., Zhang, Z., Liu, Y., and Hu, H., "An Experimental Study on the Durability of Icephobic Slippery Liquid-Infused Porous Surfaces (SLIPS) Pertinent to Aircraft Anti-/De-Icing," *2018 Atmospheric and Space Environments Conference*, AIAA Paper 2018-3654, 2018. https://doi.org/10.2514/6.2018-3654

[39] Ma, L., Zhang, Z., Gao, L., Liu, Y., and Hu, H., "An Exploratory Study on Using Slippery-Liquid-Infused-Porous-Surface (SLIPS) for Wind Turbine Icing Mitigation," *Renewable Energy*, Vol. 162, Dec. 2020, pp. 2344–2360. https://doi.org/10.1016/j.renene.2020.10.013

[40] Kreder, M. J., Alvarenga, J., Kim, P., and Aizenberg, J., "Design of Anti-Icing Surfaces: Smooth, Textured or Slippery?," *Nature Reviews Materials*, Vol. 1, No. 1, 2016, pp. 1–15. https://doi.org/10.1038/natrevmats.2015.3

[41] Nosonovsky, M., "Materials Science: Slippery When Wetted," *Nature*, Vol. 477, No. 7365, 2011, pp. 412–413. https://doi.org/10.1038/477412a

[42] Stamatopoulos, C., Hemrle, J., Wang, D., and Poulikakos, D., "Exceptional Anti-Icing Performance of Self-Impregnating Slippery Surfaces," *ACS*

Applied Materials and Interfaces, Vol. 9, No. 11, 2017, pp. 10,233–10,242. https://doi.org/10.1021/acsami.7b00186

[43] Wong, T.-S., Kang, S. H., Tang, S. K. Y., Smythe, E. J., Hatton, B. D., Grinthal, A., and Aizenberg, J., "Bioinspired Self-Repairing Slippery Surfaces with Pressure-Stable Omniphobicity," *Nature*, Vol. 477, No. 7365, 2011, pp. 443–447. https://doi.org/10.1038/nature10447

[44] Beemer, D. L., Wang, W., and Kota, A. K., "Durable Gels with Ultra-Low Adhesion to Ice," *Journal of Materials Chemistry A*, Vol. 4, No. 47, 2016, pp. 18,253–18,258. https://doi.org/10.1039/c6ta07262c

[45] Golovin, K., and Tuteja, A., "A Predictive Framework for the Design and Fabrication of Icephobic Polymers," *Science Advances*, Vol. 3, No. 9, 2017, Paper e1701617. https://doi.org/10.1126/sciadv.1701617

[46] Irajizad, P., Nazifi, S., and Ghasemi, H., "Icephobic Surfaces: Definition and Figures of Merit," *Advances in Colloid and Interface Science*, Vol. 269, July 2019, pp. 203–218. https://doi.org/10.1016/J.CIS.2019.04.005

[47] Sojoudi, H., Arabnejad, H., Raiyan, A., Shirazi, S. A., McKinley, G. H., and Gleason, K. K., "Scalable and Durable Polymeric Icephobic and Hydrate-Phobic Coatings," *Soft Matter*, Vol. 14, No. 18, 2018, pp. 3443–3454. https://doi.org/10.1039/C8SM00225H

[48] Wang, Y., Xue, J., Wang, Q., Chen, Q., and Ding, J., "Verification of Icephobic/Anti-Icing Properties of a Superhydrophobic Surface," *ACS Applied Materials and Interfaces*, Vol. 5, No. 8, 2013, pp. 3370–3381. https://doi.org/10.1021/am400429q

[49] Nosonovsky, M., and Hejazi, V., "Why Superhydrophobic Surfaces are not Always Icephobic," *ACS Nano*, Vol. 6, No. 10, 2012, pp. 8488–8491. https://doi.org/10.1021/nn302138r

[50] Ozbay, S., Yuceel, C., and Erbil, H. Y., "Improved Icephobic Properties on Surfaces with a Hydrophilic Lubricating Liquid," *ACS Applied Materials and Interfaces*, Vol. 7, No. 39, 2015, pp. 22,067–22,077. https://doi.org/10.1021/ACSAMI.5B07265/SUPPL_FILE/AM5B07265_SI_001.PDF

[51] Ma, L., Zhang, Z., Gao, L., Liu, Y., and Hu, H., "Bio-Inspired Icephobic Coatings for Aircraft Icing Mitigation: A Critical Review," *Reviews of Adhesion and Adhesives*, Vol. 8, No. 2, 2020, pp. 168–198. https://doi.org/10.7569/RAA.2020.097307

[52] Zhang, Z., Lusi, A., Hu, H., Bai, X., and Hu, H., "An Experimental Study on the Detrimental Effects of Deicing Fluids on the Performance of Icephobic Coatings for Aircraft Icing Mitigation," *Aerospace Science and Technology*, Vol. 119, Dec. 2021, Paper 107090. https://doi.org/10.1016/J.AST.2021.107090

[53] De Pauw, D., and Dolatabadi, A., "Effect of Superhydrophobic Coating on the Anti-Icing and Deicing of an Airfoil," *Journal of Aircraft*, Vol. 54, No. 2, 2017, pp. 490–499. https://doi.org/10.2514/1.C033828

[54] Huang, X., Tepylo, N., Pommier-Budinger, V., Budinger, M., Bonaccurso, E., Villedieu, P., and Bennani, L., "A Survey of Icephobic Coatings and Their Potential Use in a Hybrid Coating/Active Ice Protection System for Aerospace Applications," *Progress in Aerospace Sciences*, Vol. 105, Feb. 2019, pp. 74–97. https://doi.org/10.1016/j.paerosci.2019.01.002

[55] Gao, L., Liu, Y., Ma, L., and Hu, H., "A Hybrid Strategy Combining Minimized Leading-Edge Electric-Heating and Superhydro-/Ice-Phobic Surface Coating for Wind Turbine Icing Mitigation," *Renewable Energy*, Vol. 140, Sept. 2019, pp. 943–956. https://doi.org/10.1016/J.RENENE.2019.03.112

[56] Waldman, R. M., and Hu, H., "High-Speed Imaging to Quantify Transient Ice Accretion Process over an Airfoil," *Journal of Aircraft*, Vol. 53, No. 2, 2016, pp. 369–377. https://doi.org/10.2514/1.C033367

[57] Liu, Y., and Hu, H., "An Experimental Investigation on the Unsteady Heat Transfer Process over an Ice Accreting Airfoil Surface," *International Journal of Heat and Mass Transfer*, Vol. 122, July 2018, pp. 707–718. https://doi.org/10.1016/j.ijheatmasstransfer.2018.02.023

[58] Korhonen, J. T., Huhtamäki, T., Ikkala, O., and Ras, R. H. A., "Reliable Measurement of the Receding Contact Angle," *Langmuir*, Vol. 29, No. 12, 2013, pp. 3858–3863. https://doi.org/10.1021/la400009m

[59] Zhang, Z., Ma, L., Liu, Y., Ren, J., and Hu, H., "An Experimental Study of Rain Erosion Effects on a Hydro-/Ice-Phobic Coating Pertinent to Unmanned-Arial-System (UAS) Inflight Icing Mitigation," *Cold Regions Science and Technology*, Vol. 181, Jan. 2021, Paper 103196. https://doi.org/10.1016/j.coldregions.2020.103196

[60] Ma, L., Zhang, Z., Gao, L., Liu, Y., and Hu, H., "An Exploratory Study on Using Slippery-Liquid-Infused-Porous-Surface (SLIPS) for Wind Turbine Icing Mitigation," *Renewable Energy*, Vol. 162, Dec. 2020, pp. 2344–2360. https://doi.org/10.1016/j.renene.2020.10.013

[61] Liu, Y., Zhang, Z., Hu, H., Hu, H., Samanta, A., Wang, Q., and Ding, H., "An Experimental Study to Characterize a Surface Treated with a Novel Laser Surface Texturing Technique: Water Repellency and Reduced Ice Adhesion," *Surface and Coatings Technology*, Vol. 374, Sept. 2019, pp. 634–644. https://doi.org/10.1016/j.surfcoat.2019.06.046

[62] Meuler, A. J., Smith, J. D., Varanasi, K. K., Mabry, J. M., McKinley, G. H., and Cohen, R. E., "Relationships Between Water Wettability and Ice Adhesion," *ACS Applied Materials and Interfaces*, Vol. 2, No. 11, 2010, pp. 3100–3110. https://doi.org/10.1021/am1006035

[63] Wang, S., Chang, S., Zhao, H., and Yang, C., "Dynamic Behaviors of Water Droplet Moving on Surfaces with Different Wettability Driven by Airflow," *International Journal of Multiphase Flow*, Vol. 154, Sept. 2022, Paper 104127. https://doi.org/10.1016/J.IJMULTIPHASEFLOW.2022.104127

[64] Waldman, R. M., Li, H., Guo, H., Li, L., and Hu, H., "An Experimental Investigation on the Effects of Surface Wettability on Water Runback and Ice Accretion over an Airfoil Surface," AIAA Paper 2016-3139, 2016. https://doi.org/10.2514/6.2016-3139

[65] Cebeci, T., and Kafyeke, F., "Aircraft Icing," *Annual Review of Fluid Mechanics*, Vol. 35, No. 1, 2003, pp. 11–21. https://doi.org/10.1146/annurev.fluid.35.101101.161217

[66] Tian, L., Li, L., Hu, H., and Hu, H., "Experimental Study of Dynamic Ice Accretion Process over Rotating Aeroengine Fan Blades," *Journal of Thermophysics and Heat Transfer*, Vol. 37, No. 2, 2022, pp. 353–364. https://doi.org/10.2514/1.T6667

[67] Politovich, M. K., "Predicting Glaze or Rime Ice Growth on Airfoils," *Journal of Aircraft*, Vol. 37, No. 1, 2000, pp. 117–121. https://doi.org/10.2514/2.2570

[68] Hansman, R. J., Yamaguchi, K., Berkowitz, B., and Potapczuk, M., "Modeling of Surface Roughness Effects on Glaze Ice Accretion," *Journal of Thermophysics and Heat Transfer*, Vol. 5, No. 1, 1991, pp. 54–60.

[69] Li, L., Liu, Y., and Hu, H., "An Experimental Study on Dynamic Ice Accretion Process over the Surfaces of Rotating Aero-Engine Spinners," *Experimental Thermal and Fluid Science*, Vol. 109, Dec. 2019, Paper 109879. https://doi.org/10.1016/J.EXPTHERMFLUSCI.2019.109879

[70] Anderson, D., and Reich, A., "Tests of the Performance of Coatings for Low Ice Adhesion," *35th AIAA, Aerospace Sciences Meeting & Exhibit*, AIAA Paper 1998-0303, 1997. https://doi.org/10.2514/6.1997-303

[71] Work, A., and Lian, Y., "A Critical Review of the Measurement of Ice Adhesion to Solid Substrates," *Progress in Aerospace Sciences*, Vol. 98, April 2018, pp. 1–26. https://doi.org/10.1016/j.paerosci.2018.03.001

[72] Zhang, K., Tian, W., and Hu, H., "An Experimental Investigation on the Surface Water Transport Process over an Airfoil by Using a Digital Image Projection Technique," *Experiments in Fluids*, Vol. 56, No. 9, 2015, p. 173. https://doi.org/10.1007/s00348-015-2046-z

[73] Gao, L., Liu, Y., and Hu, H., "An Experimental Investigation on the Dynamic Glaze Ice Accretion Process over a Wind Turbine Airfoil Surface," *International Journal of Heat and Mass Transfer*, Vol. 149, March 2020, Paper 119120. https://doi.org/10.1016/J.IJHEATMASSTRANSFER.2019.119120

[74] Liu, Y., Zhang, K., Tian, W., and Hu, H., "An Experimental Study to Characterize the Effects of Initial Ice Roughness on the Wind-Driven Water Runback over an Airfoil Surface," *International Journal of Multiphase Flow*, Vol. 126, May 2020, Paper 103254.

[75] Zhang, K., and Hu, H., "An Experimental Study on the Transient Runback Characteristics of Wind-Driven Film/Rivulet Flows," *Physics of Fluids*, Vol. 33, No. 11, 2021, Paper 112104. https://doi.org/10.1063/5.0067672

[76] Hansman, R. J., and Turnock, S. S. R., "Investigation of Surface Water Behavior During Glaze Ice Accretion," *Journal of Aircraft*, Vol. 26, No. 2, 1989, pp. 140–147. https://doi.org/10.2514/3.45735

[77] Poinsatte, P. E., James, G., Fossen, V., Dewitt, K. J., Vanfossen, G. J., and Dewitt, K. J., "Convective Heat Transfer Measurements from a NACA 0012 Airfoil in Flight and in the NASA Lewis Icing Research Tunnel," *28th Aerospace Sciences Meeting*, AIAA 1990-0199, 1990. https://doi.org/10.2514/6.1990-199

L. Ukeiley
Associate Editor